# Trailing-edge dynamics of a morphing NACA0012 aileron at high Reynolds number by high-speed PIV

J. Scheller [b,a,*], M. Chinaud [a,b], JF. Rouchon [b], E. Duhayon [b], S. Cazin [a], M. Marchal [a], M. Braza [a]

[a] IMFT, Institut de Mécanique des Fluides de Toulouse, UMR CNRS-INPT-UPS No. 5502, Alleé du Prof. Camille Soula, F-31400 Toulouse, France
[b] LAPLACE, Laboratoire Plasma et Conversion d'Energie, UMR CNRS-INPT-UPS No. 5213, 2 Rue Charles Camichel, F-31071 Toulouse, France

## ABSTRACT

*Keywords:*
Morphing
Piezoelectricity
Turbulence
Shear layer
Kelvin–Helmholtz vortices
High-speed PIV

Particle image velocimetry (PIV) measurements are made at the trailing edge of a piezoelectric actuated aileron in order to investigate the physical effect on the flow via high-frequency low-amplitude actuation at high Reynolds numbers. The measurements at different actuation frequencies show the modification of the primary frequency components of the flow with the actuation frequency. A statistical analysis reveals the reduction of the Reynolds stress components which increases with the actuation frequency. Proper orthogonal decomposition (POD) analysis shows the modification of the spatial modes illustrating the vortex breakdown in the shear-layer and the reduction of the temporal mode spectral energy depending on the actuation. It has been shown that a specific low amplitude actuation frequency produces a significant reduction of the predominant shear-layer frequency.

## 1. Introduction

Today's fixed wing airfoil geometries are usually the result of a design compromise optimizing the shape only for some parts of the mission profile (McGowan et al., 1998). Control surfaces, while modifying the aerodynamic profile of the wing and thereby extending the mission profile, are usually characterized by poor aerodynamic performance and efficiency (Narcis Ursache et al., 2007). Adaptive or morphing structures hold the potential to solve this problem and studies on wing deformation are subject of much interest in the aerospace domain. Recent advances made in the field of smart-materials have renewed this interest (Namgoong et al., 2007).

The electro-active morphing for micro-air-vehicles (EMMAV) research program, which was created as part of the French foundation of "Sciences et Technologies pour l'Aéronautique et l'Espace"s' efforts to develop micro- and nano-air-vehicles and is composed of three French laboratories (IMFT, LAPLACE, ISAE), aims at optimizing the performance of micro-air-vehicles in realistic environments via electro-active morphing (Rouchon et al., 2011). During the course of this project a deformable structure was developed with embedded shape-memory alloys (SMAs) ensuring high deformation. The SMA technology, which

in the case of the EMMAV research program was composed of nickel and titanium (NITI), was able to create large deformations over a large range of stresses but was limited to a low frequency of actuation. These characteristics make it especially suitable to optimize the shape of the wing and to control the flight. The SMA actuators were activated using the Joule effect. This mechanism is well understood and was for example implemented by Barbarino et al. (2009) and Manzo (2006) in order to modify the shape of an airfoil. The developed plate allowed to study the fluid-structure coupling via wind tunnel experiments (Deri et al., 2013; Chinaud et al., 2012; Rouchon et al., 2011).

In order to control and influence the aero-elastic coupling effect inducing noise and drag, higher frequency actuation was necessary. Hence, an actuation mechanism based on piezoelectric stacks was designed. Piezoelectric actuators are capable of achieving a very high frequency of actuation (in the order of *kHz*), useful for producing a trailing-edge vortex breakdown, but only providing a very limited amount of deformation (several $\mu m$). An amplification is therefore necessary. With regard to piezoelectric stack actuators there is a diverse offering of currently available amplification mechanisms. Amplified piezoelectric stacks and flextension actuators are among the more common amplification mechanisms (Le Letty et al., 2002). The X-Frame and double X-Frame actuators developed at MIT amplify the deformation via a scissor-like mechanism (Prechtl and Hall , 1999; Hall and Prechtl, 1999; Hall et al., 2000). They were used in Boeing's SMART active flap (Straub et al., 2004). EADS optimized an amplified stack actuator to be used for the active control of a helicopter rotor (Jänker et al., 2006a,b). Finally NOLIAC developed a diamond type amplification mechanism optimized for low weight and high energy density (Mangeot et al., 2009). Since all the previously described mechanisms add a considerable amount of weight and only allow for unidirectional amplification a new `push-push` amplification mechanism was developed by Chinaud et al. (2013).

To our knowledge there are no studies in the state of the art performing a detailed experimental analysis in wind tunnel of piezoelectrically morphed devices. Previous studies focused primarily on the design and performance of the actuator and/ or the macroscopic parameters such as lift and drag coefficients (Bilgen et al., 2013; Hee, 2012). This paper will therefore focus on studying the effect of high-frequency piezoelectric actuation embedded at the trailing edge of a prototype aileron on the flow at the trailing edge via particle image velocimetry (PIV). The designed actuation mechanism allowed a deflection of the hinged trailing edge of the flap by $\pm 1.5°$ at frequencies up to 100 Hz. The experimental study allows tracking of the actuation induced modifications of the shear-layer dynamics. In this paper the actuation's effects on the flow past the trailing edge of the prototype airfoil will be investigated for three different frequencies 30 Hz, 60 Hz and 90 Hz. The instrumented model of the airfoil prototype has been tested in wind tunnel experiments by using PIV at a Reynolds number Re of 200 000. In order to further analyse the obtained velocity fields the proper orthogonal decomposition (POD) is used to identify the flow's most energetic structures in both the actuated and unactuated cases.

This work is developed as follows: in the first part we recall the fundamental properties of piezoelectric materials and the developed actuation mechanisms for the prototype aileron of 38.9 cm and at 10° angle of inclination. Subsequently the experimental set-up of the PIV measurements in the wind tunnel S4 of IMFT is described. Section 3 describes the experimental setup followed by the description of the obtained results of the PIV measurements at Re=200 000 for the piezoelectric actuation mechanism in Section 4. The static case is compared to the actuation frequencies of 30 Hz, 60 Hz and 90 Hz. Furthermore, the impact of the actuation on the turbulence spectrum and on the predominant frequency modes is analyzed for different actuation frequencies. The POD is used in Section 5 in order to identify the contribution of the actuation on the flow and identify the flows primary components. Finally the obtained results will be summarized and perspectives for future work are shown.

## 2. Actuation mechanism

### 2.1. Piezoelectric material properties

In 1880 the brothers Jacques and Pierre Curie discovered that certain types of materials became electrically polarized when subjected to a mechanical force. This effect became to be known as the direct piezoelectric effect and is nowadays exploited in variety of sensor and energy harvesting applications. The inverse effect, the deformation of the material when an electric field is applied, is used in different actuators from image stabilizers in cameras to accelerometers and elements for vibration control (Ikeda, 1990). Piezoelectric materials are defined by an electro-mechanical coupling which can be described by the following equations:

$$\{S\} = [s^E] \cdot \{T\} + [d] \cdot \{E\}, \tag{1}$$

$$\{D\} = [d] \cdot \{T\} + [\epsilon^T] \cdot \{E\}, \tag{2}$$

where $\{S\}$ is the strain vector, $[s^E]$ is the compliance matrix, $\{T\}$ is the stress vector, $[d]$ is the matrix of piezoelectric constants, $\{D\}$ is the dielectric displacement vector, $[\epsilon^T]$ is the permittivity matrix and $\{E\}$ is the electric field vector.

During the course of this work, piezoelectric stack actuators were used. These actuators are made out of several layers of piezoelectric ceramics with alternating polarity bonded together as illustrated in Fig. 1(b). This amplifies the deformation of a single piezoelectric element. The achievable deformation, $\delta_l$, of these types of actuators can be approximated by $\delta_l = P d_{33} V_e$, where $P$ is the number of layers of the stack, $d_3 3$ is the piezoelectric constant in polarization direction and $V_e$ is the applied voltage. While this actuator has a large blocking force the significant capacitance of the stacked piezoelectric elements has to be kept in mind.
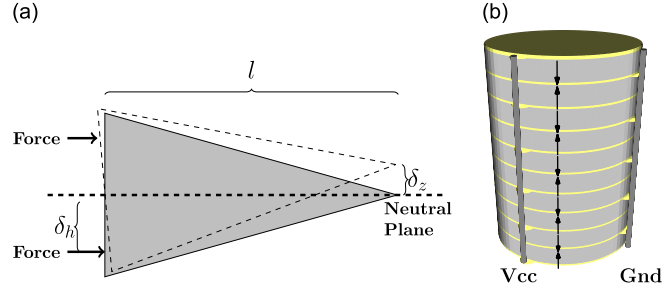
**Fig. 1.** `push-push` actuation mechanism. (a) Side view of the mechanism and (b) Illustration of a piezoelectric stack actuator.

### 2.2. Implementation

Based on the previously described piezoelectric stack actuators, an integrated actuation mechanism has been developed exploiting the benefits of the material. The proposed piezoelectric `push-push` actuation mechanism uses a lever in order to amplify the deformation of the stack actuators. By applying a force $F$ at a distance $\delta_h$ to the neutral plane the flap can be deformed by $\delta_z$ as illustrated in Fig. 1(a). By placing two stack actuators at opposing sides of the neutral plane bidirectional flapping can be achieved. Hemispheric interfaces between the flap and the actuators enable the bidirectional motion when the stack actuators are driven in 180° out of phase.

An integrated structure, shown in Fig. 2(b), has been developed containing not only the piezoelectric actuation mechanism, here described, but also the SMA based actuators. The combination of both the SMA and piezoelectric actuation mechanisms will not be detailed here as it would surpass the limits of the paper.

### 3. Experimental setup

The experiments were conducted in the wind tunnel S4 of IMFT. The dimensions of the test section are $670 \times 715$ mm. The prototype is mounted on the transversal axis of the wind tunnel with a 10° angle of inclination. The air flow is constant and directed along the $x$-axis (see Fig. 2(a)). The upstream turbulence intensity is 0.1%. Investigations were performed at ambient temperature (25 °C). In order to measure velocity field by highspeed particle image velocimetry (HSPIV), smoke particles are seeded in the air flow by a commercial smoke engine. This smoke engine is put in the upstream convergent part of the wind tunnel.

The upstream velocity field $U_\infty$ is 8 m/s. The airfoil chord length is 38.9 cm. Hence, the Reynolds number is Re = 200 000. The flap chord length is 6.9 cm. Fig. 2(a) illustrates the experimental setup. Additionally the structure is equipped with an upper and a lower shell in order to provide a form corresponding to a NACA 0012 airfoil.

A high speed camera (Photron-Fastcam RS3000) is placed to capture the particles displacement in the flow field at the end of the trailing edge of the structure. The camera is equipped with a 105 mm Nikon lens. The optical depth of field is centered on the illuminated laser sheet which corresponds to the $x$–$y$ plane. The laser pulsations are generated by a two cavities Nd:YLF (527 nm) laser (Quantronix, Darwin Duo). Using three lenses a laser sheet is generated in the $x$–$y$ plane and focalised on the investigation area. An additional mirror reflects the generated laser sheet so that the laser sheet intersects with the midsection of the structure. The thickness of the laser sheet is 2.5 mm.

In this work, the smoke particles diameter distribution, $d_p$, is centred near 3.4 μm. Particle images are recorded during the duration of the experiment using the digital high-speed camera. Each image is divided into "interrogation windows". The interrogation window size is $16 \times 16$ px$^2$ (*px* being Pixel), which corresponds to $1.79 \times 1.79$ mm$^2$, with an overlap of 50%. The most probable displacement of the particles between consecutive images and for a given interrogation window is obtained from cross-correlation plane of the consecutive images. Finally, the particle velocities in the laser sheet are simultaneously calculated from the value of the most probable displacement (depending on the size of the correlation peak) in a given interrogation window and the time delay between two laser pulses. The particle displacement during the $\pm 1.5°$ movement of the hinged flap at 30 Hz, 60 Hz and 90 Hz reflects the resulting velocity according to the deflected trailing edge position as the Stokes number ($S_k$) is much smaller than one ($S_k = \rho_p d_p^2 U_\infty / 18\mu\delta_c = 10e-3$, where $\mu$ is the dynamic viscosity of the fluid, $\rho_p$ is the density of the smoke particles and $\delta_c$ is the characteristic length). This, as suggested by Green (1995) and Samimy and Lele (1991), indicates that the particles follow the motion of the fluid.

### 4. Experimental results

The results are organized as follows: first the static case at 10° incidence is compared to the dynamic deformed cases by means of temporal averaged velocities and Reynolds stresses where the bar $\overline{x}$ indicates the time average. Then a closer look is going to be taken at the dynamics of the near-wake structure and especially the influence of the actuation on this dynamic. All physical values are made adimensional using the upstream velocity and the chord of the prototype.
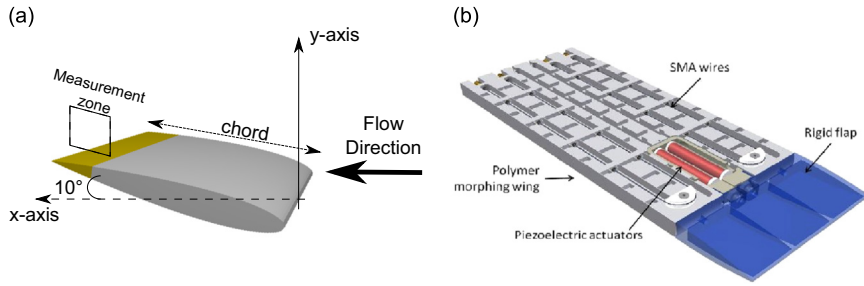
**Fig. 2.** (a) Sketch of the experimental setup and (b) 3D CAD model of the prototype.
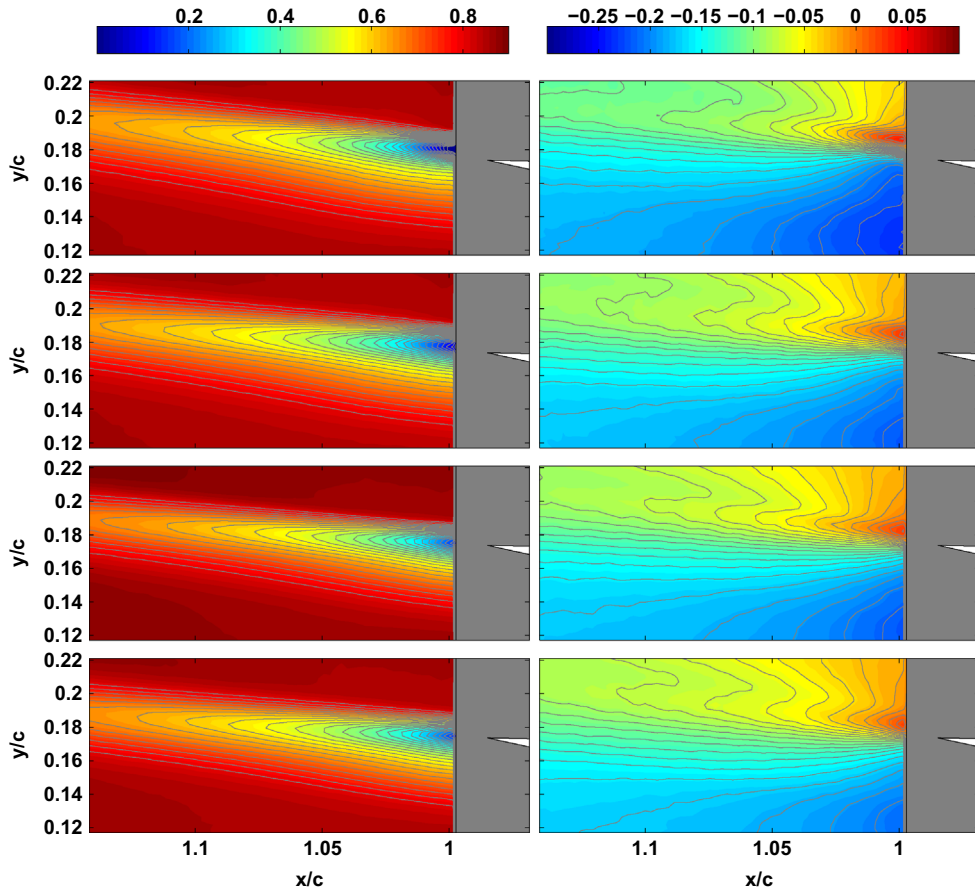


**Fig. 3.** Comparison of $\overline{U}/U_\infty$ and $\overline{V}/U_\infty$ for, from top to bottom, 0 Hz, 30 Hz, 60 Hz and 90 Hz.

### 4.1. Normalized iso-longitudinal velocity components

The piezoelectric actuation (modification of the position of the trailing edge flap) spreads the separation area of the $U$ component of the velocity in the $x$-Direction while reducing the shear-layer spread in the $y$-Direction as shown in Fig. 3(a). This is especially evident when comparing the zones of minimum velocity past the trailing edge of the piezoelectric flap.

Similarly the actuation spreads the $V$ component of the velocity in the $x$-Direction. This can be seen in Fig. 3(b). Whereas both the separation area for the $U$ and $V$ component of the velocity are horizontally stretched, the maximum or respectively minimum velocity areas past the trailing edge are reduced.

As will be shown in the next section the effects of this horizontal stretching and the reduction of the maximum/ minimum velocity areas past the trailing edge are far more apparent when comparing the normalized Reynolds stress tensors $u^2/U_\infty$, $v^2/U_\infty$ and $uv/U_\infty$.
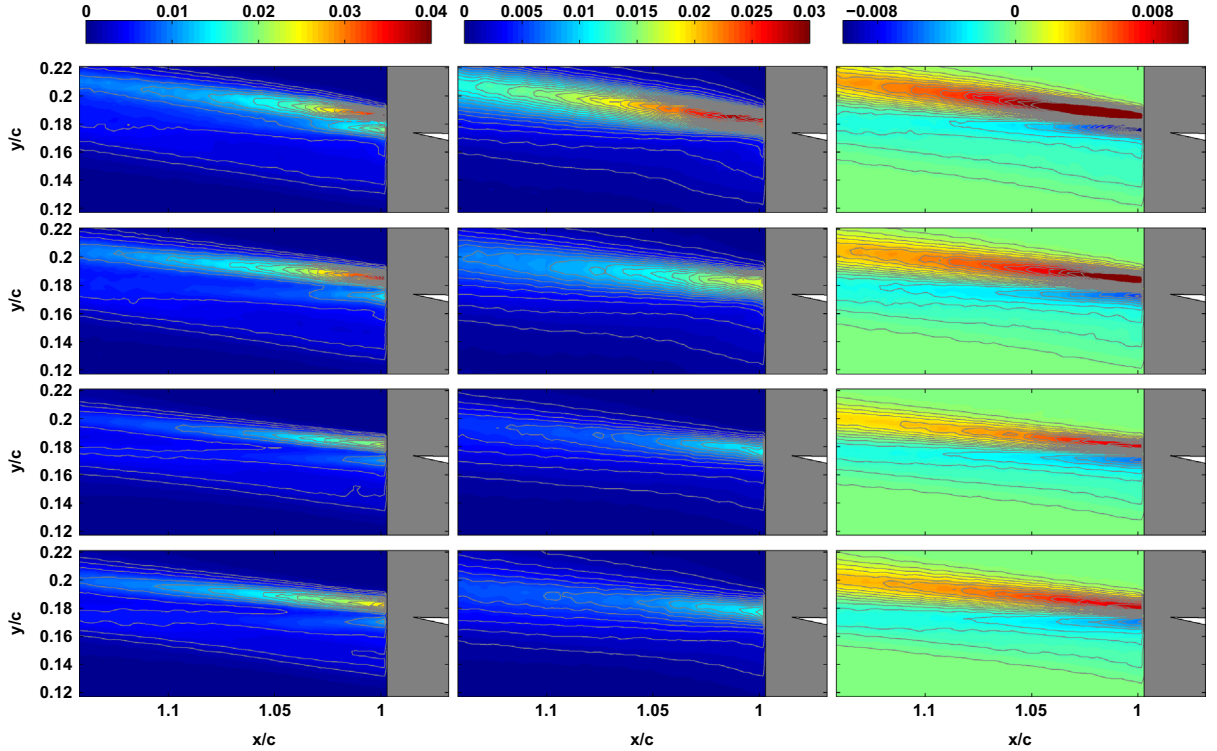
**Fig. 4.** Comparison of $\overline{u^2}/U_\infty$, $\overline{v^2}/U_\infty$ and $\overline{uv}/U_\infty$ for, from top to bottom, 0 Hz, 30 Hz, 60 Hz and 90 Hz.

### 4.2. Iso-contour of Reynolds stresses

Fig. 4(a) shows the time-averaged Reynolds stress fields of the $u^2$ component. The maximum $\overline{u^2}/U_\infty$ stress occurs in the shear layer past the trailing edge of the piezoelectric actuated flap. As the actuation frequency increases, the size of the shear layer is reduced which in turn leads to a reduction of the maximum Reynolds stress past the trailing edge of the prototype. This reduction of the shear layer is maximized at 60 Hz.

Similar to the $\overline{u^2}$ Reynolds stress field, the $\overline{v^2}/U_\infty$ field also experiences a reduction of the maximum Reynolds stress past the trailing edge of the actuated flap. Once again this reduction increases with increasing actuation frequency and is especially evident when comparing the unactuated "static" case to the actuation at 60 Hz (compare Fig. 4(b) '*top*' to the '2*nd from the bottom*'). The reduction of the $\overline{v^2}$ Reynolds stress field is even more apparent as the flap deformation is primarily in the vertical direction. Once again the maximum reduction of the $\overline{v^2}$ component of the Reynolds stresses can be observed at 60 Hz.

The shear-stress components $\overline{uv}/U_\infty$ displayed in Fig. 4(c) show a wake similar to a normal wake (Chen et al., 2008). With increasing actuation frequency both the upper and the lower wakes decrease in size up to an actuation frequency of 60 Hz.

### 4.3. Shear-layer dynamics past the trailing edge

Fig. 5 shows the spectral density of the vertical velocity component at points $x/c=1.026; y/c=0.175$, $x/c=1.033; y/c=0.172$ and $x/c=1.119; y/c=0.189$. The choice of measurement plane in the present study allows to study the interaction between the von-Kármán vortices and the shear layer past the trailing edge of the piezoelectric actuated flap. The frequency of the von-Kármán vortices $f_{VK}$ is of the order of 16.1 Hz whereas the frequency of the shear layer $f_{SL}$ is 205 Hz. The interaction between both creates $f_1=0.5f_{SL}+1.5f_{VK}$. Whereas at 10° of incidence no characteristic von-Kármán vortex street can be observed the characteristic frequency can already be observed in the energy density spectra (see Fig. 5(i)).

Comparing the vortex motion of the unactuated case with the actuated cases at 30 Hz, 60 Hz and 90 Hz shown in Fig. 6 from '*left*' to '*right*' two primary observations can be made. First the wavelet of the vortices past the trailing edge of the unactuated prototype is of the order of 0.04 m as shown in the left column of Fig. 6. Second comparing the static case to the actuated cases one can see that the turbulent energy is reduced with increasing actuation frequency $f_{act}$. This leads to a reduction of the size of the vortices and in addition leads to vortex splitting which in turn increases the turbulent energy dissipation. Whereas for the 30 Hz actuation, the coherent vortices in the shear-layer can be tracked as a function of time
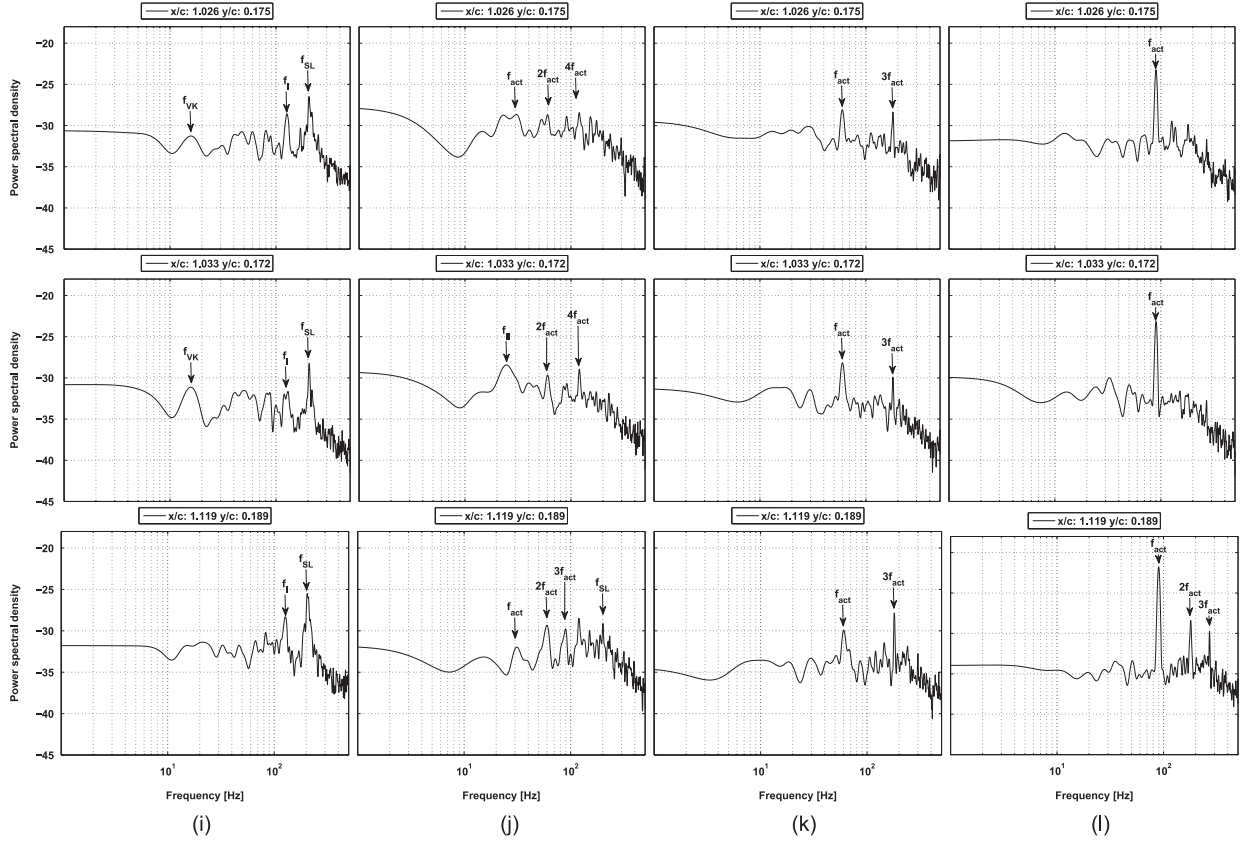
**Fig. 5.** Spectral density of *V* for from left to right 0 Hz, 30 Hz, 60 Hz and 90 Hz at positions $x/c$: 1.024 $y/c$: 0.170 (*top*), $x/c$: 1.033 $y/c$: 0.170 (*middle*) and $x/c$: 1.089 $y/c$: 0.170 (*bottom*).

(see Fig. 6), for the higher actuation frequencies the size and coherence of the vortices is considerably reduced. This coincides well with the previously discussed Reynolds stress fields.

This reduction of turbulent energy can be best explained by taking a look at the energy spectra for the different positions and actuation frequencies as shown in Fig. 5. The spectra compare the unactuated case to the actuated cases at different frequencies. Even small actuation frequencies induce a shift in the characteristic frequencies of the energy spectra whereas for 30 Hz the actuation frequency itself is not predominant but rather its harmonics (see Fig. 5(j)). With increasing actuation frequency this phenomena changes and the actuation frequency itself becomes predominant. Nevertheless, the harmonics can still be observed in the energy spectra (see Fig. 5(k) and (l)). At 90 Hz the actuation frequency supersedes all other frequencies as shown in Fig. 5(l).

Generally speaking one can say that the frequencies higher $f > f_{act}$ are attenuated. Nevertheless the lower frequencies are also influenced as was shown with the modification of $f_{VK}$. This effect increases with the increasing amount of kinetic energy that is added to the flow, in other words with increasing actuation frequency. When comparing the energy density levels of the frequencies of interest ($f_{VK}$, $f_{SL}$ and the actuation frequencies) one can see how the energy seeded into the flow focuses the energy of the flow onto the frequency of actuation. Even though this is not directly apparent for 30 Hz of actuation the influence of the actuation is undeniable. Furthermore, if one considers the reduction of the average value of the frequency peaks to be the actuation objective one can conclude that 60 Hz of actuation is more beneficial than 90 Hz. This also agrees very well with the Reynolds stress fields shown in the previous section.

In order to take a closer at the actuation effects on the flow the next section will decompose the flow in proper orthogonal modes to identify for each actuation frequency the most energetic structures.

## 5. Modal analysis

As stated in the previous section the purpose of this part of the paper is to analyze the behavior of the flow at different actuation frequencies using a POD analysis. The goal of the POD is to decompose the flow in coherent structures or events containing the majority of the information describing the physics of the flow. It has proven to be an effective method in identifying the dominant features in both experimental and numerical data. Regarding turbulence, the POD was first introduced by Lumley (1967) but several researchers have mentioned this method previously independent of each other (for
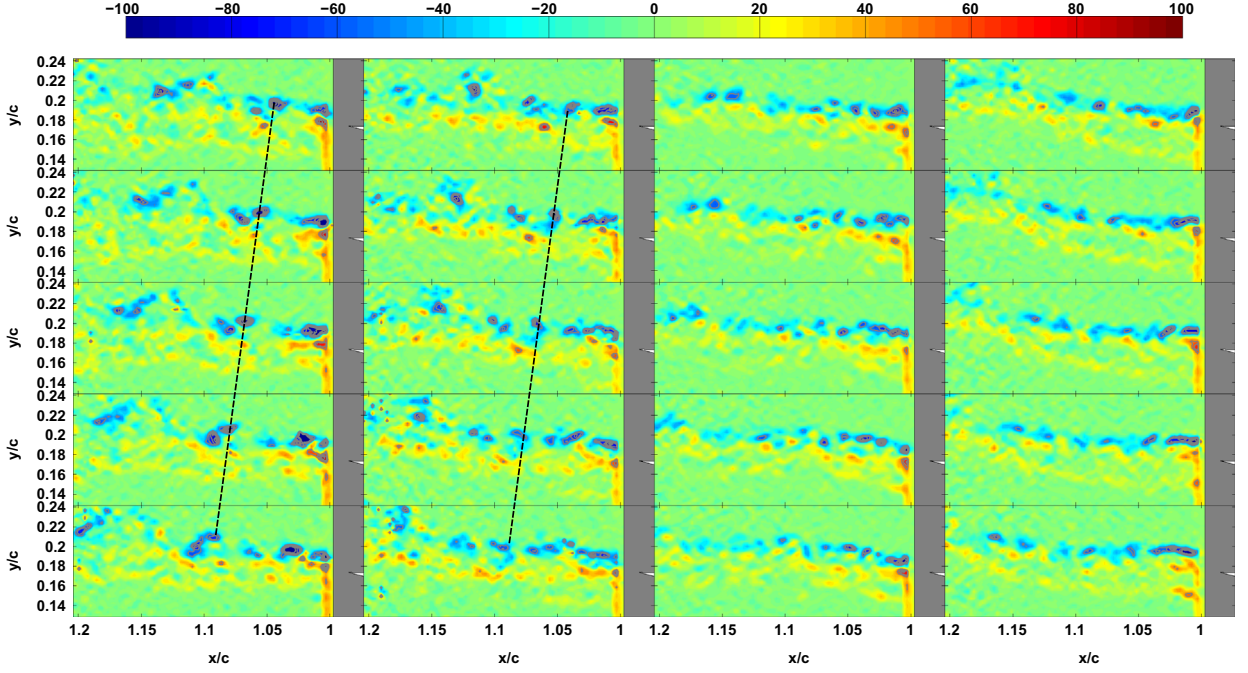
**Fig. 6.** Sequence of vortex motion ($\Delta t = 0.001$) for the unactuated case and the actuation frequencies 30 Hz, 60 Hz and 90 Hz (from *left* to *right*).

an exhaustive review please refer to Berkooz et al., 1993). Nowadays the POD is not only used to identify coherent structures and events but also in data reduction in order to construct low-dimensional models (Kostas et al., 2005). The POD decomposes the flow $U'(x, t)$ in $N$ spatial $\phi_i(x)$ and temporal modes $a_i(t)$ according to their energy content as illustrated in the following equation:

$$U'(x, t) = \sum_{i=1}^{N} \phi_i(x) a_i(t). \tag{3}$$

This decomposition can be done using several methods. The results presented in this paper are based on a snapshot based method as described by Perrin (2005), which is especially suitable for applications with experimental data:

$$u^{i^T} = \begin{bmatrix} u_1 & u_2 & u_3 & \cdots & u_{N_X} & v_1 & v_2 & v_3 & \cdots & v_{N_X} \end{bmatrix}. \tag{4}$$

Given a set of $N$ instantaneous velocity fields $u^i$ obtained via PIV as given in Eq. (4) where $N_X = nx \cdot ny$ is the number of points in the cartesian coordinate system and $u_j$ and $v_j$ are the normal and streamwise velocities at point $i$, respectively. We can construct a snapshot matrix $M$ as given in the following equation:

$$M = [u^1 \ u^2 \ \cdots \ u^N] = \begin{bmatrix} u_1^1 & u_1^2 & \cdots & u_1^{N-1} & u_1^N \\ u_2^1 & u_2^2 & \cdots & u_2^{N-1} & u_2^N \\ \vdots & \vdots & \vdots & \vdots & \vdots \\ u_{N_X}^1 & u_{N_X}^2 & \cdots & u_{N_X}^{N-1} & u_{N_X}^N \\ v_1^1 & v_1^2 & \cdots & v_1^{N-1} & v_1^N \\ v_2^1 & v_2^2 & \cdots & v_2^{N-1} & v_2^N \\ \vdots & \vdots & \vdots & \vdots & \vdots \\ v_{N_X}^1 & v_{N_X}^2 & \cdots & v_{N_X}^{N-1} & v_{N_X}^N \end{bmatrix}. \tag{5}$$

The decomposition can now be performed based on the correlation matrix $R$ which can be written as

$$R = \frac{1}{N} M^T \cdot M, \tag{6}$$

and hence the eigenvalue problem is given as

$$RA = \lambda A \tag{7}$$

with the eigenvalues $\lambda$ and the eigenvector $A$. After rearranging the eigenvalues such that

$$\lambda_1 > \lambda_2 > \cdots > \lambda_N = 0 \tag{8}$$

we can calculate the spatial modes $\phi_i$ as given in the following equation:

$$\phi_i = \frac{\sum_{j=1}^{N} A_j^i u^j}{\left\| \sum_{j=1}^{N} A_j^i u^j \right\|}, \quad i = 1, 2, \ldots, N. \tag{9}$$

The temporal modes can now be calculated by projecting the snapshot matrix onto the previously calculated spatial modes:
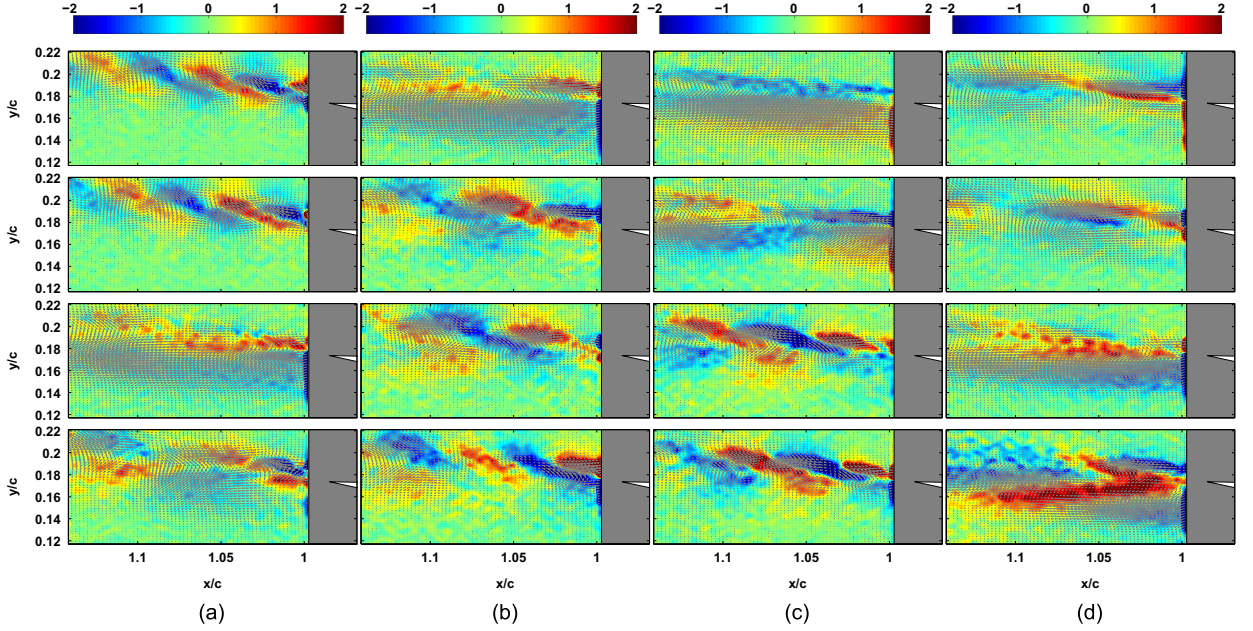
$$a_i = \phi_i M \tag{10}$$



**Fig. 7.** Vorticity with superposed velocity vectors in gray comparing the first four spatial modes for the different analyzed actuation frequencies from top to bottom. (a) 0 Hz, (b) 30 Hz, (c) 60 Hz and (d) 90 Hz.
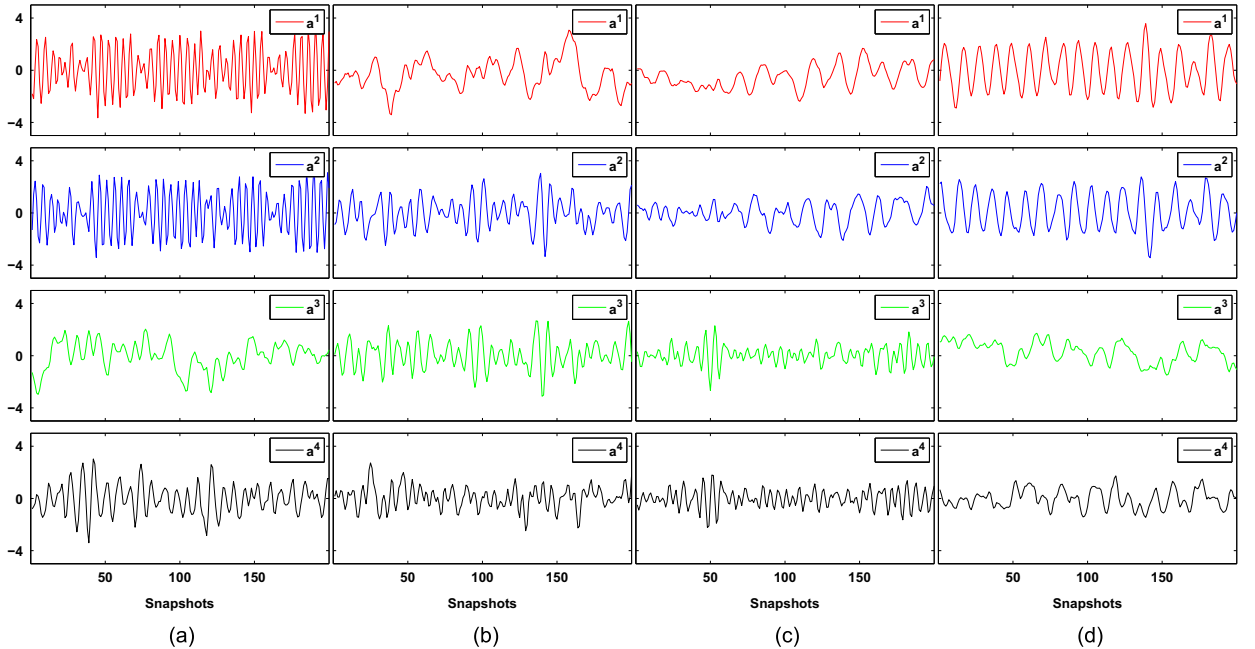


**Fig. 8.** Comparison of the first four temporal modes for the different analyzed actuation frequencies from top to bottom. (a) Temporal modes 0 Hz, (b) 30 Hz, (c) 60 Hz and (d) 90 Hz.
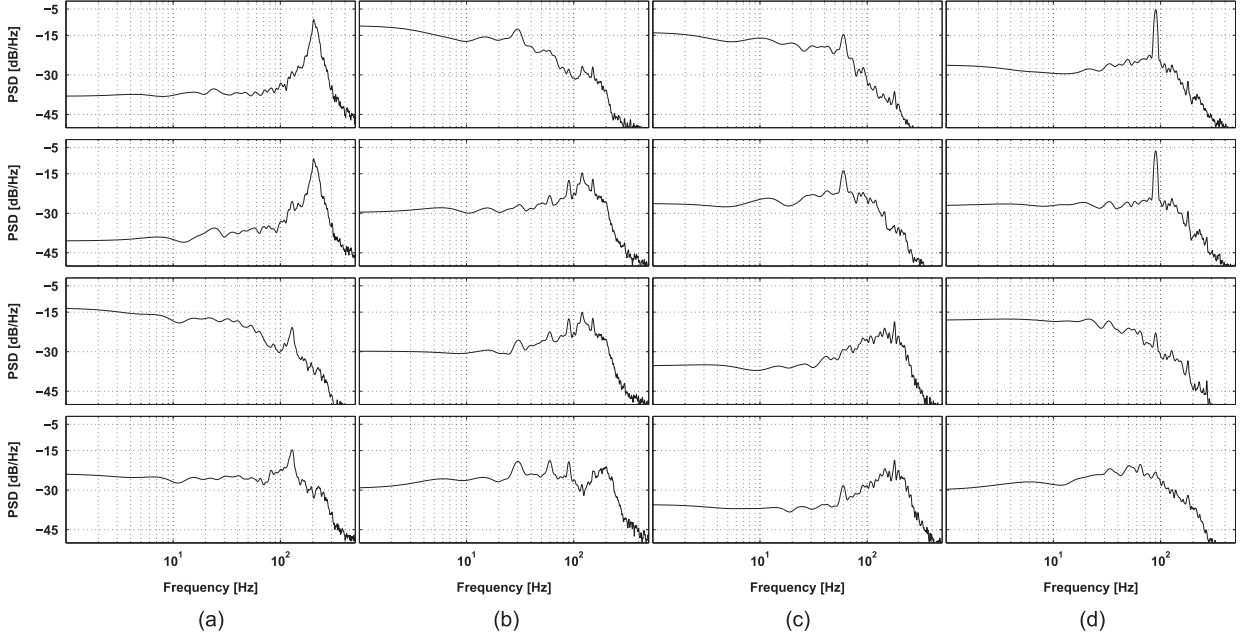
**Fig. 9.** Comparison of the PSDs of the first four temporal modes for the different analyzed actuation frequencies from top to bottom. (a) 0 Hz, (b) 30 Hz, (c) 60 Hz and (d) 90 Hz.

Both the temporal and spatial modes can now be used in order to reconstruct a snapshot $u^n$:

$$u^n = \sum_{i=1}^{N} a_i^n \phi_i. \tag{11}$$

Fig. 7 shows the first four vorticity modes with superposed velocity vectors. The modification of the flow is highlighted when comparing the first four vorticity modes of the unactuated case in Fig. 7(a) to the cases at actuation frequencies 30 Hz, 60 Hz and 90 Hz (Fig. 7(b, c, and d) respectively). The actuation introduces additional modes which supersede the frequency of the shear layer. At 30 Hz of actuation an interaction between the shear layer and the actuation frequency can be observed. The energy density at the shear layer frequency $f_{SL}$ is reduced significantly at higher actuation frequencies, $f_{act} > 30$ Hz.

The temporal modes (shown in Fig. 8) and their energy density spectra (shown in Fig. 9) underline this behavior. As explained in the previous section one can see that energy seeded into the flow using the piezoelectric actuation focuses the flows spectral energy on the respective actuation frequency (compare Fig. 9(a–d)). Furthermore one can see that the overall energy density level is reduced for 30 Hz and 60 Hz of actuation whereas the energy density level at 90 Hz is increased when compared to the unactuated case.

## 6. Conclusion

The goal of this study was to show the effect on the flow of a low amplitude, high frequency piezoelectric actuation mechanism integrated in an airfoil prototype. The design of the hybrid prototype was illustrated and the piezoelectric actuation mechanism was explained. Using this prototype it was shown that the energy induced via the actuation of the piezoelectric stack actuators has a considerable impact on the shear-layer vortex structures. The actuation frequency of the piezoelectric `push-push` actuation mechanism can clearly be identified in the energy-density spectra. By exploiting these mechanisms one can possibly attenuate the high-frequency Kelvin–Helmholtz vortices, which are a major source for noise. Furthermore this study identified an optimum open-loop actuation frequency of 60 Hz by comparing the Reynolds stress fields and energy density spectra for the different actuation frequencies. It can be noticed that the use of piezoelectric actuators for the modification of the trailing-edge vortices is an original state of the art innovation. A POD analysis highlighted the influence of the low-amplitude piezoelectric actuation on the temporal and spatial modes.

Future investigations will focus on the simultaneous drag and noise reduction by associating different kinds of electroactive materials.

The obtained results show that a specific low-amplitude actuation frequency produces a significant reduction of the predominant shear-layer frequencies which, to our knowledge, is a novelty in the state of the art.

# Acknowledgements

# References

Barbarino, S., Pecora, R., Lecce, L., Concilio, A., Ameduri, S., Calvi, E., 2009. A novel SMA-based concept for airfoil structural morphing. Journal of Materials Engineering and Performance 18 (5), 696–705.

Berkooz, G., Holmes, P., Lumley, J.L., 1993. The proper orthogonal decomposition in the analysis of turbulent flows. Annual Review of Fluid Mechanics 25 (1), 539–575.

Bilgen, O., Landman, D., Friswell, M.I., 2013. Low Reynolds number behavior of a solid-state piezocomposite variable-camber wing. AIAA Journal 1515, 8–11.

Chen, Y., Matalanis, C.G., Eaton, J.K., 2008. High resolution PIV measurements around a model turbine blade trailing edge film-cooling breakout. Experiments in Fluids 44 (2), 199–209.

Chinaud, M., Boussaid, A., Rouchon, J., Duhayon, E., Deri, E., Harribey, D., Braza, M., 2012. Thermo-mechanical coupling in Nitinol. Application to an electro-morphing plate. In: XXth International Conference on Electrical Machines (ICEM). IEEE, pp. 2580–2584.

Chinaud, M., Scheller, J., Rouchon, J.F., Duhayon, E., Braza, M., 2013. Hybrid electroactive wings morphing for aeronautic applications. Solid State Phenomena 198, 200–205.

Deri, E., Braza, M., Cid, E., Cazin, S., Michaelis, D., Degouet, C., 2014. Investigation of the three-dimensional turbulent near-wake structure past a flat plate by tomographic PIV at high Reynolds number. Journal of Fluids and Structures 47, 21–30. ISSN 0889-9746, 10.1016/j.jfluidstructs.2012.11.005, URL: ⟨http://www.sciencedirect.com/science/article/pii/S0889974612002095⟩.

Green, S.I. (Ed.), Fluid Vortices: Fluid Mechanics and Its Applications, vol. 30. , Springer Science & Business Media. URL: ⟨http://www.springer.com/materials/mechanics/book/978-0-7923-3376-0?otherVersion=978-94-010-4111-9⟩.

Hall, S.R., Prechtl, E.F., 1999. Preliminary testing of a Mach-scaled active rotor blade with a trailing-edge servo flap. In: 1999 Symposium on Smart Structures and Materials. International Society for Optics and Photonics, pp. 14–21.

Hall, S.R., Tzianetopoulou, T., Straub, F.K., Ngo, H.T., 2000. Design and testing of a double X-frame piezoelectric actuator. In: SPIE's 7th Annual International Symposium on Smart Structures and Materials. International Society for Optics and Photonics, pp. 26–37.

Hee, K.H., 2012. Designing Morphing Airfoils for Improving the Aerodynamic Characteristics.

Ikeda, T., 1990. Fundamentals of Piezoelectricity. Oxford University Press.

Jänker, P., Claeyssen, F., Grohmann, B., Christmann, M., Lorkowski, T., Leletty, R., Sosniki, O., Pages, A., 2006a. New actuators for aircraft and space applications. In: 10th International Conference on New Actuator.

Jänker, P., Hermle, F., Friedl, J., Lentner, K., Enenkl, B., Müller, C., 2006. Advanced piezoelectric servo flap system for rotor active control. In: 32nd European Rotorcraft Forum. Maastricht, The Netherlands.

Kostas, J., Soria, J., Chong, M., 2005. A comparison between snapshot pod analysis of piv velocity and vorticity data. Experiments in Fluids 38 (2), 146–160.

Le Letty, R., Lhermet, N., Patient, G., Claeyssen, F., Lang, M., 2002. Valves Based on Amplified Piezoelectric Actuators. online (retrieved 20.06.11). URL: http://www.cedrat.com/fileadmin/user-upload/cedrat-groupe/Publications/Publications/2002/06/Actuator2002-A4-6-VALVES-BASED-ON-AMPLIFIED-PIEZOELECTRIC-ACTUATORS.pdf.

Lumley, J.L., 1967. The structure of inhomogeneous turbulent flows. In: Atmospheric Turbulence and Radio Wave Propagation, pp. 166–178.

Mangeot, C., Andersen, B., Hilditch, R., 2009. New actuators for aerospace. In: Conference on Piezoelectric Actuation at the Institute of Mechanical Engineers (IMechE), vol. 22, London.

Manzo, J.E., 2006. Analysis and Design of a Hyper-elliptical Cambered Span Morphing Aircraft Wing (Ph.D. thesis). Cornell University.

McGowan, A.-M.R., Wilkie, W.K., Moses, R.W., Lake, R.C., Florance, J.P., Wieseman, C.D., Reaves, M.C., Taleghani, B.K., Mirick, P.H., Wilbur, M.L., 1998. Aeroservoelastic and structural dynamics research on smart structures conducted at NASA langley research center. In: 5th SPIE International Symposium on Smart Structures and Materials, San Diego, CA.

Namgoong, H., Crossley, W.A., Lyrintzis, A.S., 2007. Aerodynamic optimization of a morphing airfoil using energy as an objective. AIAA Journal 45 (9), 2113–2124.

Narcis Ursache, Tomas Melin, Askin Isikveren, Mike Friswell, 2007. Morphing winglets for aircraft multi-phase improvement. In: 7th AIAA ATIO Conference, 2nd CEIAT International Conference on Innovation and Integration in Aerospace Sciences, 17th LTA Systems Tech Conference; followed by 2nd TEOS Forum. Aviation Technology, Integration, and Operations (ATIO) Conferences. American Institute of Aeronautics and Astronautics, September 2007. URL: http://dx.doi.org/10.2514/6.2007-7813.

Perrin, R., 2005. Analyse physique et modélisation d'écoulements incompressibles instationnaires turbulents autour d'un cylindre circulaire à grand nombre de Reynolds (Ph.D. thesis).

Prechtl, E.F., Hall, S.R., 1999. Design of a high efficiency, large stroke, electromechanical actuator. Smart Materials and Structures 8 (1), 13.

Rouchon, J.-F., Harribey, D., Derri, E., Braza, M., 2011. Activation d'une voilure déformable par des câbles d'AMF répartis en surface. 20ème Congrès Français de Mécanique, 28 août/2 September 2011-25044 Besançon, France (FR).

Samimy, M., Lele, S., 1991. Motion of particles with inertia in a compressible free shear layer. Physics of Fluids A: Fluid Dynamics (1989–1993) 3 (8), 1915–1923.

Straub, F.K., Kennedy, D.K., Stemple, A.D., Anand, V., Birchette, T.S., 2004. Development and Whirl Tower test of the SMART Active Flap Rotor. San Diego, CA, USA, March.